Magnetic Resonance in Medicine 55:659–668 (2006)

Automated In Vivo Segmentation of Carotid Plaque MRI with Morphology-Enhanced Probability Maps

Fei Liu,[1]* Dongxiang Xu,[1] Marina S. Ferguson,[1] Baocheng Chu,[1] Tobias Saam,[1] Norihide Takaya,[1] Thomas S. Hatsukami,[2] Chun Yuan,[1] and William S. Kerwin[1]

MRI is a promising noninvasive technique for characterizing atherosclerotic plaque composition in vivo, with an end-goal of assessing plaque vulnerability. Because of limitations arising from acquisition time, achievable resolution, contrast-to-noise ratio, patient motion, and the effects of blood flow, automatically identifying plaque composition remains a challenging task in vivo. In this article, a segmentation method using maximum a posteriori probability Bayesian theory is presented that divides axial, multi-contrast-weighted images into regions of necrotic core, calcification, loose matrix, and fibrous tissue. Key advantages of the method are that it utilizes morphologic information, such as local wall thickness, and coupled active contours to limit the impact from noise and artifacts associated with in vivo imaging. In experiments involving 142 sets of multi-contrast images from 26 subjects undergoing carotid endarterectomy, segmented areas of each of these tissues per slice agreed with histologically confirmed areas with correlations (R^2) of 0.78, 0.83, 0.41, and 0.82, respectively. In comparison, manually identifying areas blinded to histology yielded correlations of 0.71, 0.76, 0.33, and 0.78, respectively. These results show that in vivo automatic segmentation of carotid MRI is feasible and comparable to or possibly more accurate than manual review for quantifying plaque composition. Magn Reson Med 55: 659–668, 2006. Published 2006 Wiley-Liss, Inc.†

Key words: in vivo; carotid artery; multi-contrast MR; plaque composition; naïve-Bayesian network

Numerous studies have shown that MRI exhibits high contrast for internal plaque features, but that combined information from multiple contrast weightings is critical for distinguishing all plaque components (1–6). Based on these studies, desirable combinations of contrast weightings and a set of image characteristics have emerged that can be used to segment plaque into its subcomponents. Manual segmentation using these characteristics has produced quantitative measurements of the relative volumes of necrotic cores, calcification, loose matrix, and fibrous tissue that correlate strongly with histologic assessments (5).

Nevertheless, replacing subjective, manual segmentation with an automated segmentation alternative would have several benefits. Aside from saving time in image review, automated segmentation would reduce the considerable amount of training required to read these images and the corresponding inter-rater variability. Additionally, a viable, automated segmentation procedure would permit various combinations of contrast weightings and image characteristics to be objectively analyzed for accuracy in plaque characterization. Such studies have been conducted using automated segmentation of ex vivo endarterectomy specimens (6,7), but these results are difficult to translate to in vivo imaging, given the different constraints regarding acquisition time, resolution, contrast-to-noise ratio, and effects of blood flow. Recent efforts to demonstrate in vivo segmentation of some plaque components (8,9) are promising, but they have not yet been histologically validated.

The goal of this work was to develop a flexible, multi-contrast plaque segmentation technique that is suitable for objectively testing various approaches for measuring plaque composition in vivo and to validate the method with histology. Furthermore, the technique was developed to mimic the highly successful procedure used in manual review. Unlike other works (6,8,9) in which only the intensity values in each contrast weighted image were considered, and (7) in which spatial information was used just for minimizing pixel discontinuity, in this study, we consider morphologic distribution information as an important factor to make the final decision. We, therefore, refer to this method as "Morphology-Enhanced Probabilistic Plaque Segmentation" (MEPPS). We hypothesize that the MEPPS approach increases the accuracy in the segmentation result.

MATERIALS AND METHODS

Study Population

A total of 31 consecutive patients scheduled for carotid endarterectomy (CEA) were imaged on a GE Signa 1.5T MR scanner to obtain images with T1 (TR = 800ms, TE = 11ms), T2 (TR = 3150ms, TE = 66ms), proton density (PD; TR = 2770ms, TE = 9.3ms), time-of-flight (TOF; TR = 23ms, TE = 2.8ms), and contrast-enhanced (CE) T1 (TR = 800ms, TE = 11ms) weightings at 10 contiguous locations, centered at the carotid bifurcation (10). CE-T1W images were acquired approximately 10 min after injection of 0.1 mmol/kg of a gadolinium contrast agent (Omniscan, Amersham Health, now part of GE Healthcare). In-plane resolution was 0.63 mm, resulting in a pixel size of 0.31 mm after zero-filled interpolation, and the slice thickness was 2.0 mm. All subjects gave informed consent and the study was approved by the institutional review board.

At endarterectomy, the plaque was removed intact, formalin fixed, embedded en-Cbloc in paraffin, and serially

[1]Department of Radiology, University of Washington, Seattle, WA, USA.
[2]Department of Surgery, VA Puget Sound Health Care System and University of Washington, Seattle, WA, USA.
Grant Sponsor: NIH; Grant Numbers: R01-HL056784 and R44-HL070576.
Correspondence to: Fei Liu, Ph.D., The Vascular Imaging Lab, University of Washington, 815 Mercer Street, Box 358050, Seattle, WA 98109, USA.
E-mail: feil@u.washington.edu
Received 9 August 2005; revised 19 October 2005; accepted 18 November 2005.
DOI 10.1002/mrm.20814
Published online 7 February 2006 in Wiley InterScience (www.interscience.wiley.com).

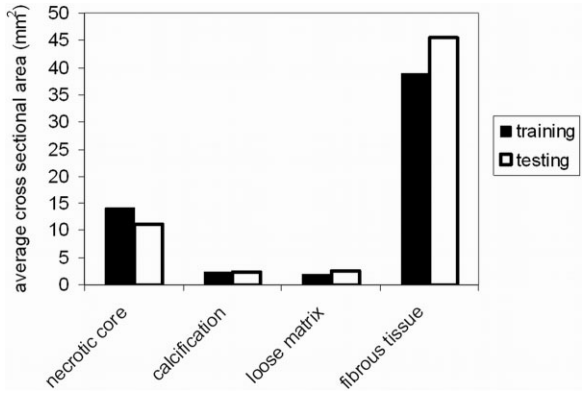

FIG. 1. Distribution of plaque components in the testing and training data sets.

sectioned at 1.0 mm intervals in the common carotid and at 0.5 mm intervals throughout the bulb and internal carotid. After staining with Hematoxylin and Eosin, histology sections were matched to MR images using the bifurcation, lumen size and shape, and calcifications as landmarks. The sections were digitized and regions of necrotic core (including intraplaque hemorrhage), calcification, and loose matrix, were outlined using an in-house program. Loose matrix included all tissues that were loosely woven, such as proteoglycan rich fibrous matrix, organizing thrombus, and granulomas. All un-outlined remaining tissue was considered as dense fibrous matrix.

Ground Truth Generation

As in previous work (2,5), MR images were graded on a subjective, 5-level image quality scale, where subjects scoring below 3 had poorly defined vessel boundaries and were eliminated from the study. Five subjects were excluded for poor image quality. From the remaining 26 subjects, a total of 142 locations (each physical location consists of 5 images representing all 5 different contrast weightings) were selected for the study, where the remaining locations either extended beyond the limits of the histologic specimen or had damaged histology. To generate ground truth for training and evaluation of the segmentation algorithm, images from all 26 subjects were manually segmented based on established MRI criteria (5) and knowledge of the histologic results. The review was conducted by an expert radiologist (BC) in conjunction with the histologist (MSF) using the manual drawing feature of our quantitative MR analysis tool, CASCADE (11). As in histology, 3 types of tissue—calcification, necrotic core, and loose matrix—were identified, and the remainder was assigned to fibrous tissue.

From this data set, 14 subjects (84 locations) were assigned to a training set and 12 subjects (58 locations) were assigned to a testing data set. The latter 12 subjects were selected for testing because these 12 had previously been included in an evaluation of manual drawing (5). Algorithm performance on these 12 subjects could thus be directly compared to manual drawing. The average size of each tissue type was confirmed to be similar between training and testing groups (Fig. 1).

Segmentation Algorithm

The 84 locations in the training set were used to train the MEPPS algorithm, which was integrated into CASCADE. The MEPPS algorithm first determines the probability that each pixel belongs to each of the 4 tissue types. Then, competing active contours (12) are used to identify the boundaries of high-probability regions for each tissue type. The flowchart of major steps for assessing tissue composition in this study is shown in Fig. 2.

In designing the MEPPS algorithm, we further attempted to mimic the thought process used by the radiologist in manual review. First, manual review generally relies on relative intensities (e.g., hyper, hypo, or isointense) to describe image features. We, therefore, preprocess the images to establish a baseline iso-intensity for each image and scale all pixel values relative to this baseline. Second, reviewers use morphologic cues, such as local wall thickness, in addition to intensity when classifying regions. We, therefore, assign probability based on both intensity and morphology. Finally, reviewers intuitively use the most value-added contrast weightings in classifying regions, ignoring potentially confounding information from low-value weightings. We, therefore, sought to identify the most useful weightings for segmentation.

Pre-Processing

Major hurdles for in vivo plaque analysis compared to ex vivo analysis are that in vivo images are subject to patient motion, intensity inhomogeneities, and variable absolute intensities depending on relative coil placement. In vivo images must be registered, the intensity must be adjusted relative to a uniform baseline, and the wall region must be identified. Because of superior flow suppression from its double inversion recovery preparation, T1W is generally the best contrast weighting for identifying the lumen and wall boundaries. Therefore, we standardized our approach to trace the lumen and outer wall boundaries of the common or internal carotid arteries on only the T1W images. These boundaries were traced manually.

Subsequently, images from the remaining 4 weightings were registered to the T1W images to overcome patient motion between acquisitions. Registration used the active edge maps framework (13) to identify an in-plane shift that best aligned edge pixels in the non-T1W images with the lumen and wall contours drawn on the T1W image. Edge

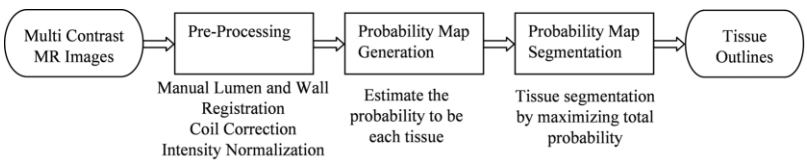

FIG. 2. Flowchart of MEPPS algorithm based plaque tissue segmentation.

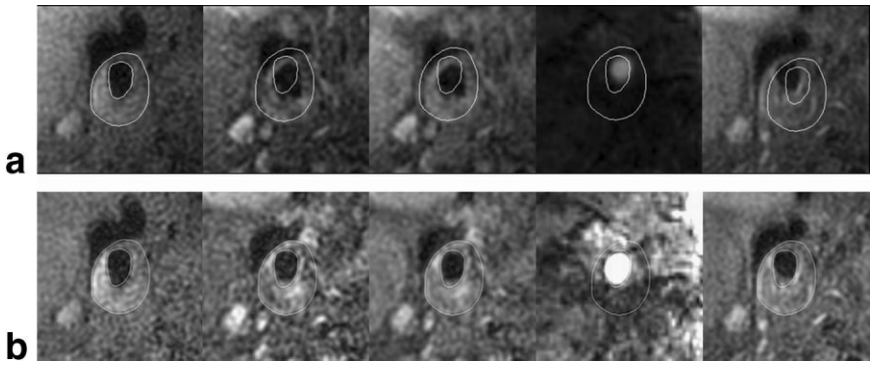

FIG. 3. Preprocessing results (the displayed images are 4 cm × 4 cm): (**a**) multi-contrast images (left to right: T1, T2, PD, TOF, CET1) demonstrating poor alignment of contours in the original MR images; (**b**) resultant images after registration and intensity normalization.

pixels were found using Canny edge detection (14). For this image set, 87% of all images were properly registered automatically. The remainder required additional manual shifts to achieve the best alignment of contours with image features. As a result of registration, proper alignment of image pixels was restored. Additionally, the wall boundaries were mapped to the remaining contrast weightings, precluding the need to draw boundaries on all contrast weightings.

After registration, the effects of coil inhomogeneity were eliminated by dividing each image by a smooth, estimated sensitivity profile. We estimate the sensitivity profile within a 4 cm × 4 cm region of interest aligned with the center of the wall contour using an adaptive thresholding technique (15) that simultaneously estimates the profile in all image weightings assuming they are related by a scalar multiple. In that method, under a Neumann boundary condition, the profile u was estimated from observed signal g by solving the partial differential equation:

$$\Delta\log(u) + \lambda(\log(u) - \log(g)) \times \exp(-(\log(u) - \log(g))^2/\sigma^2) = 0 \quad [1]$$

After dividing by the estimated profile, intensity is uniform within the region.

To normalize the absolute intensity, each image weighting is divided by its median intensity within the region. This approach is based on the common practice of using the adjacent sternocleidomastoid muscle or fibrous tissue to identify an isointense reference for gauging signal intensity in manual review (5). The median intensity was chosen because, in general, fibro-muscular regions occupy a large portion of the region and the remainder is more or less equally divided between bright and dark regions. Thus, the median intensity is highly likely to fall within a fibro-muscular region, whereas the mean intensity is highly dependent on the distribution between bright and dark pixels. Additionally, this approach was tested for T1, T2, PD, TOF, and CET1 weightings and, on average, the mean ratio between sternocleidomastoid muscle intensity and the median intensity in the 4 cm × 4 cm region was found to be 1.07 with an SD of 0.11. Because the median value is easily obtained without the need to detect a reference region and closely agrees with the sternocleidomastoid muscle intensity, in this study, we used it as the baseline intensity. Examples of the effects of pre-processing are shown in Fig. 3.

Probability Map Generation

The core task of the MEPPS algorithm is to assign 4 probabilities to each pixel. These probabilities represent the likelihood that the pixel is necrotic core, calcification, loose matrix, or fibrous tissue. We base this probability on the pixel intensity in each contrast weighting—represented by the vector **x**—and on 2 morphologic factors: the local wall thickness t and the distance of the pixel from the lumen d. Thus, we determine the probability $\Pr(T_i \mid t,d,x)$, where Ti corresponds to one of the 4 tissue types (i.e., i = 1,2,3,4). The 2 distances t and d capture information about the local plaque morphology, typically used in manual review. For example, thin plaque regions are generally fibrous and loose matrix is most commonly seen adjacent to the lumen (16).

To estimate each probability, we can assume that the intensity of a given tissue does not vary with position in the plaque. For example, calcification has the same appearance whether it is adjacent to the lumen or deep within the plaque. Thus, **x** is conditionally independent of t and d, given T_i. This assumption allows us to cast the probability as a naïve-Bayesian network (17) (see Appendix) and leads to the formula:

$$\Pr(T_i|t,d,x) = \frac{p(t,d|T_i)p(x|T_i)\Pr(T_i)}{\sum_{j=1}^{4} p(t,d|T_j)p(x|T_j)\Pr(T_j)} \quad [2]$$

The 2 conditionally independent probability density functions (PDFs) $p(x \mid T_i)$ and $p(t,d \mid T_i)$, and the relative frequency of each of the 4 tissue types $\Pr(T_i)$, were estimated from the training set. Factoring the probability in this way greatly reduces the required size of the training set and eliminates the need to estimate $\Pr(T_i \mid t,d,x)$ directly, which makes it possible to combine more features together given a limited data set (17).

To estimate the PDFs from the training set of 84 locations, the Parzen window method (18) was used. In this method, a smooth PDF is estimated from a finite data set by using a Gaussian kernel to blur each data point in space. For $p(x \mid T_i)$, we found that a Gaussian kernel of width σ = 0.07 and computation of the PDF on a 5-dimensional grid with 10 intensity levels per contrast weighting produced a smooth, self-consistent PDF. From this estimate, the PDF at an arbitrary point in space is computed using linear

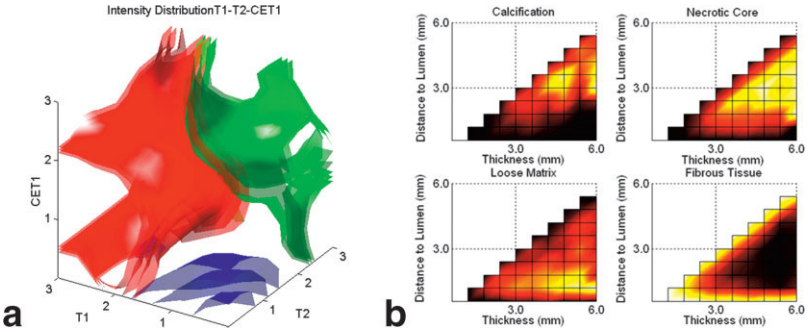

FIG. 4. Probability distributions: (**a**) normalized intensity of T1, T2, and contrast-enhanced (CE) T1-weighted images for calcification (blue), necrotic core (red), and loose matrix (green). Three isosurfaces of probability are shown for each tissue type corresponding to probabilities of 0.3, 0.45, and 0.6. (**b**) Probabilities for each tissue type given plaque thickness and distance to the lumen (ranging from low probability in black to high probability in yellow).

interpolation over the grid. To estimate $p(t,d \mid T_i)$, the Parzen window method was also used with $\sigma = 0.09$ and 11 levels in the range of 0 to 6 mm.

Contour Generation

Once the probabilities for each pixel are determined, the final step is to classify each pixel as a given tissue. Although the pixels could be classified based on the highest probability alone, we utilize a competing contour formulation to define the final regions. This additional step provides two benefits. First, it provides the ability to easily edit the regions by modifying the contours; and second, it helps to eliminate isolated pixels and convoluted regions attributable to noise.

The contours delineating each tissue region are determined using the active region method (12). Each of 4 contours seeks 1 pre-assigned tissue. In order to produce reasonable boundaries, contours are moving under a smoothness constraint to maximize the total probability for the corresponding tissue within it. Based on Gibbs-Markov random field theory (19,20), using the level set method to represent each contour, the energy functional is designed as:

$$E(\Phi_i) = \sum_{i=1}^{4} \int\int_{\Omega} -\log(\Pr(T_i))H(\Phi_i)dxdy + \lambda_1 \sum_{i=1}^{4} \int\int_{\Omega} |\nabla H(\Phi_i)|dxdy + \lambda_2 \int\int_{\Omega} \left(\sum_{i=1}^{4} H(\Phi_i) - 1 \right)^2 dxdy \quad [3]$$

where Φ_i is the level set function and $H(\Phi)$ is the Heaviside function. The first item sums probability within the contours, the second one is a measure of total contour length, and the third one constrains each pixel to belong to one and only one contour. By using the level set method, topology changes of the curves are handled automatically, allowing individual contours to split and merge to form as many distinct regions as necessary. More detailed numerical implementation of the level set method can be found in (12,21–24). Based on our experience, to avoid severe shrinkage, λ_1 was set relatively small to 0.01, and λ_2 was set to 2.25, which satisfies both region partition and numerical stability.

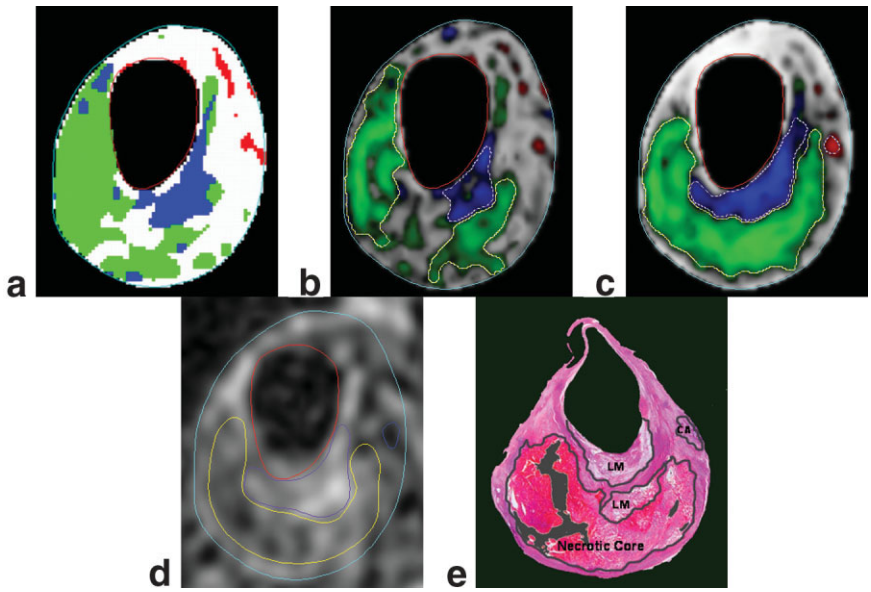

FIG. 5. Segmentation results showing: (**a**) automatic labeling result by Gaussian classifier; (**b**) probability map and region contours based on intensity only, with necrotic core in green, calcification in red, loose matrix in blue, and fibrous tissue in gray; (c) corresponding results including morphologic information; (**d**) manual segmentation result displayed on T2-weighted image; and (**e**) corresponding histology specimen used to guide contour placement in (d) (dark regions within histology specimen are artifacts due to sectioning).

Validation

The MEPPS algorithm was validated using the 58 locations from 12 subjects in the testing data set. The algorithm was applied using all 5 contrast weightings and compared to the histologically confirmed drawings. As an additional comparison, we also performed segmentation using only intensity information, by deleting the morphology-based terms from the probability computation in Eq. [2]. This allowed us to assess the contribution of morphology to overall performance.

For validation, we used two metrics. First, we examined the correlations between histologically measured areas of plaque tissue and the estimates from MRI for each of the 58 locations in the testing group. This reflects the fundamental goal of quantifying plaque composition. Then, to evaluate the performance of the segmentation routine itself, we assessed the pixel-wise accuracy of the segmentation results compared to the contours drawn manually with a histologic reference.

For both assessments, we also compared the performance of MEPPS to the results of manual review and a common, maximum-likelihood Gaussian classifier. Manual results were generated by another expert radiologist (TS) blinded to the histologic results and served as a benchmark for comparing the performance of the segmentation algorithm to established manual performance (5). The Gaussian classifier was obtained by fitting 5-dimensional Gaussian distributions to the observed intensities for each tissue class in the training set. In the testing set, each pixel was assigned to the class that exhibited the highest probability based on the Gaussian model. This approach is similar to the minimum distance to means classifier previously employed for ex vivo segmentation of carotid plaque (6), with the exception that in the Gaussian classifier, the distance to the mean is effectively weighted by the SD of the distribution.

RESULTS

PDF Estimation

The results of probability density modeling are shown in Fig. 4. For clearer visualization, we transformed the density function $p(\mathrm{x} \mid T_i)$ into the true probability $\Pr(T_i \mid \mathrm{x})$ (see Appendix for relationship) and projected it onto a 3-dimensional subspace considering only 3 contrast weightings T1-T2-CET1. This figure demonstrates generally good separation of the 3 tissues shown in image intensity space. High probabilities for calcification are located in the corner where intensity is low in each contrast weighting. Loose matrix is located where T2 intensity is high and CET1 is relatively higher than T1 intensity. Necrotic core exhibits high probabilities where T1 intensity is high and CET1 is isointense. In T2W images, the necrotic core exhibits a broad distribution of intensities, indicating that contrast weighting is of limited use for detecting necrotic core. This supports the previous conclusion in (5) that, depending on the amount and age of hemorrhage present within the necrotic core, signal varies in T2W images. Fibrous tissue, which is not shown, is diffusely distributed among these regions.

Tissue probabilities conditional on morphology $\Pr(T_i \mid t,d)$ are also shown in Fig. 4. The triangular region of support reflects the fact that the distance to the lumen cannot exceed the local thickness of the plaque. The high probability (bright) area for necrotic core is located in the central portion of high thickness regions, and fibrous tissue is likely located near the lumen and wall boundaries. The high probability area for loose matrix is relatively close to the lumen in thick plaque regions. Calcification is most common far from the lumen surface.

Segmentation Results—Qualitative

Figure 5 shows the results of segmentation of the example of Fig. 3 based on probabilities. Results with and without the additional morphologic information are displayed as are the histology-guided manual drawings, the results of Gaussian classification, and the corresponding histology section. To visualize the pixel-wise probabilities in Figs. 5b and 5c, each pixel has been color coded to indicate the tissue with the highest probability. The intensity represents the difference between the highest and second highest probabilities, essentially providing a confidence metric in the classification. Also shown are the final contours delineating the tissue regions.

From this example, three aspects are apparent. First, intensity-based techniques (a and b) achieved similar results. Secondly, the benefits of morphologic information are apparent by noting that without morphologic information, the necrotic core is incorrectly divided into two disjoint regions and a region of necrotic core is incorrectly identified in a thin-walled region near the top of the image. Finally, the use of active contour methods to delineate the final regions has successfully overcome the presence of "holes" in the probability map that might otherwise have been misclassified.

In Fig. 6, a poorly segmented example is shown for comparison, which shows that residual misregistration contributes to the remaining disagreement between MEPPS and histology. In this case, the in-plane shift was able to restore alignment of most features in the plaque, but one area of calcification remained offset in the PD and T1-weighted images. As a result, the calcification was missed and the area was grouped into the adjacent necrotic core. In other instances, small regions were missed due to through-plane motion, which led to corresponding regions being out of plane. This kind of mismatch may also result in an overestimate or underestimate of the tissue area for correctly detected tissues, such as the necrotic core in the example.

Segmentation Results—Quantitative

For overall validation, we examined the correlation between automatic and histology-guided manual segmentation. The areas of each tissue type in each of the 58 test locations were used for comparison, and the results are compiled in Table 1. The overall performance of the non-parametric intensity-based segmentation is generally similar to the Gaussian classifier, with the exception that identifying calcification is significantly improved with the non-parametric technique. The benefits of using morphol-

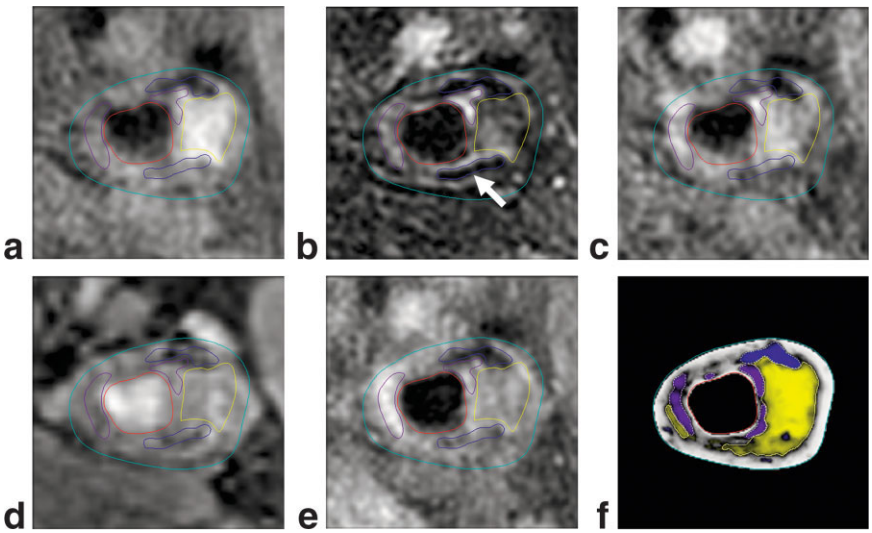

FIG. 6. An example of poor segmentation results for calcification: (**a**)-(**e**) histology guided manual drawing displayed on T1, T2, PD, TOF, and CET1, respectively; (**f**) MEPPS segmentation result in which a calcified region (arrow in b) was missed.

ogy in addition to intensity are apparent, given the higher correlations for MEPPS compared to either of the results based on intensity alone.

When comparing the results of MEPPS with histology guided drawing, we found the correlation for necrotic core and fibrous tissue to be relatively high. This is partially due to the fact that typical areas of necrotic core and fibrous tissue are larger than calcifications or loose matrix. Nevertheless, calcification attained a high correlation because it is well-defined in histology and by MRI. The lower correlation for loose matrix can be attributed to its small size and the fact that it represents an aggregate of multiple possible tissues that may have slightly different MRI properties. We observed that misclassification of loose matrix was generally associated with fibrous tissue, which is not surprising given that loose matrix is actually a sub-class of fibrous tissue. Furthermore, if we combine the two into a combined fibrous group, we achieve a correlation of 0.85 with histology.

The classification accuracies for all pixels in the testing set are tabulated in Table 2 in terms of sensitivity and specificity. Values for automated and blinded manual segmentation are similar, with both exhibiting high specificities for all tissue types and high sensitivity for fibrous tissue. Sensitivities for necrotic core and calcifications are good, whereas loose matrix has relatively low sensitivity. The somewhat lower sensitivities can be attributed in large part to this metric being pessimistic for small regions, such as most calcifications and loose matrix. This observation is illustrated by the fact that the segmentation result in Fig. 5 exhibits excellent qualitative agreement with the histology-guided result. However, in this example, the sensitivity for detecting calcified pixels is only 0.37 and that for loose matrix is only 0.73. This discrepancy is due to the fact that for small regions, slight differences in the location of contours can lead to a large percentage of pixels that do not overlap.

Bland-Altman plots comparing MEPPS and histology for each tissue are provided in Fig. 7. These illustrate the generally good agreement between MEPPS and histology. No significant biases were detected. Additionally, the error appears unrelated to the size of the region and no size-dependent biases are apparent.

Optimal Contrast Weightings

To explore the performance of the MEPPS algorithm when fewer than 5 contrast weightings were available, we performed segmentation with all combinations of 4, 3, 2, and 1 contrast weightings. As a performance metric, we used the sum of the correlations for all 4 tissue types and ranked the preferred combinations from highest to lowest. Additionally, we utilized the training data in this evaluation to incorporate more locations. Because of this, the absolute correlations may be somewhat elevated, but the relative merits of different weightings should be accurately represented. Fig. 8 shows the relative number of appearances each contrast weighting made in the top performing contrast combinations according to the sum of correlation R^2 for 4 types of tissues. For example, in the top 10 combinations, T1 appeared 9 times, CET1 appeared 8 times, T2 and

Table 1
Correlations (R^2) of Histology-Guided Measurements (total area per location) with Manual Segmentation, Gaussian Segmentation, Intensity-Based Automatic Segmentation, and MEPPS

Tissue	Manual	Gaussian	Intensity-based	MEPPS
Necrotic core	0.71	0.65	0.61	0.78
Calcification	0.76	0.64	0.78	0.83
Loose matrix	0.33	0.28	0.32	0.41
Fibrous tissue	0.78	0.71	0.69	0.82

Table 2
Pixel-Wise Segmentation Accuracy

	MEPPS		Manual	
	Sensitivity	Specificity	Sensitivity	Specificity
Necrotic core	0.75	0.92	0.64	0.90
Calcification	0.65	0.98	0.77	0.97
Loose matrix	0.51	0.97	0.37	0.99
Fibrous tissue	0.88	0.78	0.84	0.68

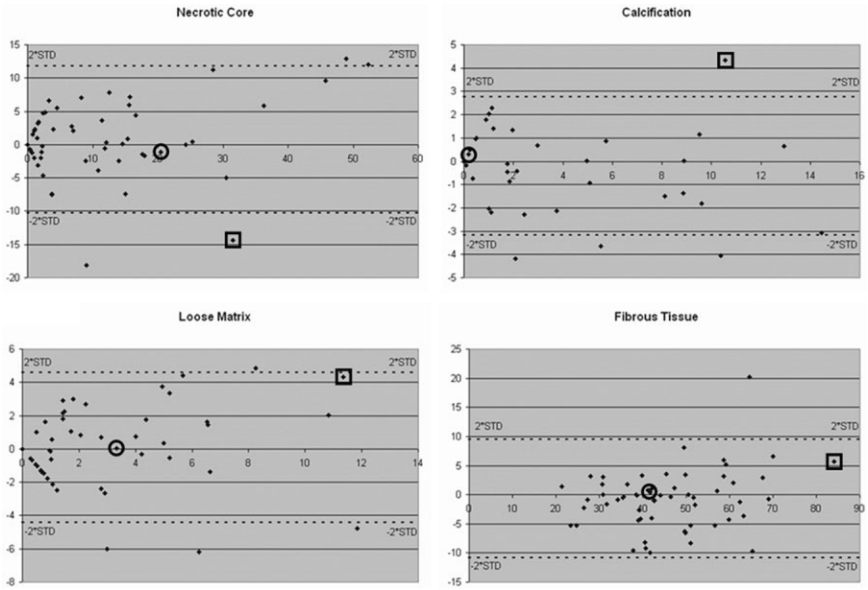

FIG. 7. Bland-Altman plots of each tissue for MEPPS segmentation result versus histology guided manual segmentation. The vertical axes show the histology results minus the MEPPS results in mm^2, and the horizontal axes show the average results for each location in the study. The square marks the poorly segmented example in Fig. 6 and the circle marks the example of Fig. 5.

TOF each appeared 7 times, and PD appeared only 6 times. This figure illustrates that T1 is the most important contrast weighting for proper segmentation and PD is relatively unimportant. The contributions of T2, TOF, and CET1 appear similar.

The best performing combinations for 4, 3, 2, and 1 contrast weightings are listed in Table 3. Note that no combination outperforms the use of all 5 weightings, although the performance remains quite good even when only 3 weightings are available. As expected, the performance with only 1 contrast weighting is poor. Table 4 shows for comparison the best performing combinations in the absence of CET1 images. This result suggests that without the use of a contrast agent, T2-weighted images fill the role of CET1 images and give generally similar, although slightly diminished, performance.

DISCUSSION

This study establishes that accurate division of atherosclerotic plaque into 4 constitutive components can be accomplished with in vivo MRI and automated segmentation with the MEPPS algorithm. Division of the plaque into 4 components was based on the 4 principal components investigated by Saam et al. (5), in which the ability to use MRI to comprehensively quantify plaque composition was validated with histology. In that investigation, intraplaque hemorrhage was also measured as a sub-component of the necrotic core. Here, necrotic cores represented both hemorrhagic cores and lipid-rich cores without hemorrhage. In previous studies, hemorrhagic and lipid-rich necrotic cores have been grouped under the term "soft plaque components" (2). Because of the limited size of the data set, we chose not to segment intraplaque hemorrhage as a distinct entity. Nevertheless, extension of the algorithm to identify intraplaque hemorrhage remains a future goal.

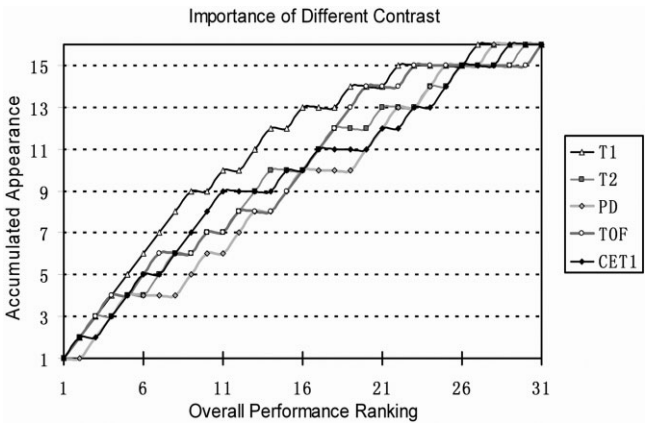

FIG. 8. Accumulated appearance of each contrast weighting along overall performance ranking.

Among the detected tissues, loose matrix got the lowest correlation with histology guided segmentation. Nevertheless, the correlation coefficient (R) was 0.64 (R^2 = 0.41), which is close to the value of 0.7 reported for manual outlining (5). The difficulty in identifying loose matrix by any means is due in part to the fact that regions classified as loose matrix by MRI are not well-defined histologically. By histology, loose matrix includes all tissues that are loosely woven, such as proteoglycan-rich fibrous matrix, organizing thrombus, and granulomas. Also, as mentioned in (5), "Loose matrix areas were generally small in size, and their often juxtaluminal location complicates differentiation from flow artifacts." To address the poorer performance for loose matrix, we investigated grouping it with fibrous tissue to form 3 basic plaque groups: fibrous, necrotic, and calcified. With this definition, MEPPS exhibited values of R^2 near 0.8, or R near 0.9, for all plaque components.

This approach for segmenting carotid plaque MRI has several advantages particular to this application. First, the use of morphologic information in the segmentation procedure is a powerful addition to intensity information, which reflects the observed spatial distribution of plaque components. Furthermore, use of a Bayesian network to

Table 3
List of Best Overall Performance (R^2) with Combinations of 5-1 Contrast Weightings

Best combination of contrast weightings	Necrotic core	Calcification	Loose matrix	Fibrous tissue	Overall*
T1-T2-PD-TOF-CET1	0.85	0.86	0.59	0.87	3.17
T1-T2-TOF-CET1	0.82	0.84	0.61	0.86	3.13
T1-TOF-CET1	0.81	0.84	0.58	0.83	3.06
T1-CET1	0.81	0.82	0.50	0.84	2.97
T1	0.83	0.55	0.17	0.81	2.36

*Overall performance score based on sum of individual tissue correlations.

implement morphology-based segmentation has its own advantages. Such naïve-Bayesian classifiers have outperformed many more sophisticated classifiers, especially where the features are not strongly correlated (25). Most notably, using this framework reduces the required size of the training data set, as illustrated by the following scenario. Suppose a given pixel should be classified as calcification. In order for this to occur, a general classifier would have to have encountered a pixel in the training set with a similar intensity in a similar relative location. In the naïve-Bayesian classifier, the training set would only have to contain a pixel with a similar intensity and any other pixel in a similar relative location. Clearly, in a limited data set, the latter scenario is much more likely.

Additionally, this approach has advantages over previously proposed segmentation methods based on clustering (7,8). In clustering methods, the exact number of regions must be specified a priori. Also, the possibility of two regions of the same component with different intensity characteristics due to different mixtures of subcomponents is not well handled. In this case, the two regions will typically be assigned to different clusters. Thus, clustering methods generally require the number of clusters to be over-specified and then rely on region merging to generate the final result. In Bayesian approaches, such as MEPPS, on the other hand, the ranges of intensities are modeled statistically. Also, although MEPPS assumes 4 tissue types may be present, the ultimate number of regions and tissue types at any one location is arbitrary.

Another advantage of this approach is the use of nonparametric PDF estimates as opposed, for example, to assuming a Gaussian distribution. This allows the high-probability region to distribute in space in any shape, determined only by the training data. One implication is that the method is fairly robust to misregistration and motion artifacts in the image. The PDF is trained on data containing these artifacts and, thus, learns to recognize them. For example, high probability for calcification may be assigned as long as the majority of contrast weightings exhibit a dark pixel. In the PDF, such rules would be represented by extensions of high-probability regions that are not easily modeled parametrically. We attribute the relatively worse performance of the Gaussian classifier in detecting calcifications to this effect. Generally small in size, calcifications are among the most sensitive to residual misregistration errors.

A final advantage of this approach is the use of active contours to perform the final region classification. As demonstrated by example, the active contours help overcome segmentation errors caused by isolated pixels with low confidence in the probability estimates. Although not addressed in this study, the use of contours to represent the regions may also facilitate manual editing of the results. While all of these advantages arise from specific challenges posed by carotid MRI, other segmentation problems could, nevertheless, benefit from some of these same approaches.

Comparison of the performance of segmentation with different combinations of contrast weightings also provided an objective means of comparing the relative merits of different weightings. Notably, PD was found to provide little information for segmentation and might be eliminated from the protocol to save time. Also, TOF imaging showed surprising importance, possibly because it reduces the likelihood that inclusion of a small region of the lumen would be mislabeled as calcification. In TOF, the lumen is characteristically bright. The comparison also supports the previous observation by Wasserman et al. (26) that T2 and CET1 weightings provide largely similar information on plaque composition. In fact, the slightly better performance of the algorithm when CET1 was used instead of T2 supports their assertion that CET1 exhibits better signal-to-noise performance. Overall, these results suggest that a rapid protocol generating only T1, CET1, and possibly TOF weightings might go a long way toward plaque characterization. Additionally, use of more contrast weightings can at times lead to worse performance

Table 4
List of Best Overall Performance (R^2) with Combinations of 4-1 Contrast Weightings, Excluding CET1

Best combination of contrast weightings	Necrotic core	Calcification	Loose matrix	Fibrous tissue	Overall*
T1_T2_PD_TOF	0.84	0.87	0.53	0.86	3.10
T1_T2_TOF	0.83	0.82	0.54	0.86	3.05
T1_T2	0.81	0.78	0.49	0.84	2.92
T1	0.83	0.55	0.17	0.81	2.36

*Overall performance score based on sum of individual tissue correlations.

because the additional weightings may introduce more image artifacts or other sources of noise.

One limitation of this technique is that it represents only one of several steps in carotid plaque analysis. We break the analysis into 4 basic steps: lumen boundary detection, outer wall boundary detection, multi-contrast registration, and finally, plaque segmentation. This investigation primarily addresses the final step of plaque segmentation. The remaining steps demand new and improved automated techniques as well. Nevertheless, we consider plaque segmentation as the most critical step for automation. Previous work has been directed at lumen detection (27), wall detection (7), and registration (13). Additionally, manually tracing internal plaque composition is considerably more tedious and less reproducible than tracing the boundaries (28). Although manual oversight and input will be required until all aspects of plaque analysis can be automated, the use of MEPPS for plaque segmentation can considerably increase the speed of reviewers performing carotid plaque analysis.

CONCLUSIONS

This study shows that automatic segmentation of in vivo carotid MRI—a long-time goal—is achievable. Segmented regions of necrotic core, calcification, loose matrix, and fibrous tissue were identified, with performance metrics similar to and generally slightly better than corresponding manual review. Thus, automatic segmentation can be implemented as an aid to measuring plaque composition by MRI. These measurements can in turn be used to investigate the association of plaque features with plaque vulnerability or the changes in plaque composition over time, due to therapy.

APPENDIX

The derivation of these methods makes frequent use of Bayes' theorem for conditional probabilities. Specifically, the following relationships are used:

1. By using intensity information **x** itself, the post-probability, is

$$\Pr(T_i|x) = \frac{p(x|T_i)\Pr(T_i)}{p(x)} = \frac{p(x|T_i)\Pr(T_i)}{\sum_{j=1}^{4} p(x|T_j)\Pr(T_j)} \quad [A1]$$

2. By using morphologic intensity, specifically (*t, d*) itself, the post-probability is

$$\Pr(T_i|t,d) = \frac{p(t,d|T_i)\Pr(T_i)}{p(t,d)} = \frac{p(t,d|T_i)\Pr(T_i)}{\sum_{j=1}^{4} p(t,d|T_j)\Pr(T_j)} \quad [A2]$$

3. Combining intensity information and morphologic information together, the final post-probability is

$$\Pr(T_i|t,d,x) = \frac{p(t,d,x|T_i)\Pr(T_i)}{p(t,d,x)} = \frac{p(t,d,x|T_i)\Pr(T_i)}{\sum_{j=1}^{4} p(t,d,x|T_j)\Pr(T_j)} = \frac{p(x|T_i)p(t,d|T_i)\Pr(T_i)}{\sum_{j=1}^{4} p(x|T_j)p(t,d|T_j)\Pr(T_j)} \quad [A3]$$

REFERENCES

1. Shinnar M, Fallon JT, Wehrli S, Levin M, Dalmacy D, Fayad Z, Badimon JJ, Harrington M, Harrington E, Fuster V. The diagnostic accuracy of ex vivo MRI for human atherosclerotic plaque characterization. Arterioscler Thromb Vasc Biol 1999;19:2756–2761.
2. Yuan C, Mitsumori LM, Ferguson MS, Polissar NL, Echelard D, Ortiz G, Small R, Davies JW, Kerwin WS, Hatsukami TS. In vivo accuracy of multispectral magnetic resonance imaging for identifying lipid-rich necrotic cores and intraplaque hemorrhage in advanced human carotid plaques. Circulation 2001;104:2051–C2056.
3. Mitsumori LM, Hatsukami TS, Ferguson MS, Kerwin WS, Cai J, Yuan C. In vivo accuracy of multisequence MR imaging for identifying unstable fibrous caps in advanced human carotid plaques. J Magn Reson Imaging 2003;17:410–420.
4. Cappendijk VC, Cleutjens KB, Kessels AG, Heeneman S, Schurink GW, Welten RJ, Mess WH, Daemen MJ, van Engelshoven JM, Kooi ME. Assessment of human atherosclerotic carotid plaque components with multisequence MR imaging: initial experience. Radiology 2005;234: 487–492.
5. Saam T, Ferguson MS, Yarnykh VL, Takaya N, Xu D, Polissar NL, Hatsukami TS, Yuan C. Quantitative evaluation of carotid plaque composition by in vivo MRI. Arterioscler Throm Vas 2005;25:234–239.
6. Clarke SE, Hammond RR, Mitchell JR, Rutt BK. Quantitative assessment of carotid plaque composition using multi-contrast MRI and registered histology. Magn Reson Med 2003;50:1199–1208.
7. Itskovich VV, Samber DD, Mani V, Aguinaldo JGS, Fallon JT, Tang CY, Fuster V Fayad ZA. Quantification of human atherosclerotic plaques using spatially enhanced cluster analysis of multicontrast-weighted magnetic resonance images. Magn Reson Med 2004;52:515–523.
8. Adame IM, Geest RJ, Wasserman BA, Mohamed MA, Reiber JH, Lelieveldt BP. Automatic segmentation and plaque characterization in atherosclerotic carotid artery MR images. MAGMA 2004;16:227–34.
9. Liu F, Xu D, Yuan C, Kerwin WS. In vivo carotid plaque tissue segmentation using probability maps and multiple active contour competition. In: Proceedings of the 13th Annual Meeting of ISMRM, Miami Beach, FL, USA, 2005. p 1746.
10. Yarnykh VL, Yuan C. Unit 1.4: high-resolution multi-contrast MRI of carotid artery wall for plaque evaluation. 2004. In: Haacke EM, editor. Current protocols in magnetic resonance imaging. 1st ed. New York: Wiley. p. A1.4.1–A1.4.18.
11. Xu D, Kerwin WS, Saam T, Ferguson M, Yuan C. CASCADE: computer aided system for cardiovascular disease evaluation. In: Proceedings of the 12th Annual Meeting of ISMRM, Kyoto, Japan, 2004. p. 1922.
12. Paragios N, Deriche R. Coupled geodesic active regions for image segmentation: a level set approach. ECCV, Dublin, Ireland, 2000. p. 224–240.
13. Kerwin WS, Yuan C. Active edge maps for medical image registration. Proceedings of SPIE 2001;4322:516–526.
14. Canny J. A computational approach to edge detection. IEEE T Pattern Anal 1986;8:679–698.
15. Liu F, Luo Y, Song X Hu D. An active surface model based adaptive thresholding algorithm by repulsive external force. SPIE, J Electron Imaging 2003;12:299–306.
16. Burke AP, Kolodgie FD, Farb A, Weber DK, Malcom GT, Smialek J, Virmani R. Healed plaque ruptures and sudden coronary death: evidence that subclinical rupture has a role in plaque progression. Circulation 2001;103:934–940.
17. Hecherman D. 1999. A tutorial on learning with Bayesian networks. M. Jordan, editor. In: Learning in graphical models. Cambridge, MA: MIT Press.
18. Parzen E. On the estimation of a probability density function and the mode. Ann Math Stat 1962;33:1065–1076.

19. Geman S, Geman D. Stochastic relaxation, Gibbs distributions, and the Bayesian restoration of images. IEEE T Pattern Anal 1984;6:721–741.
20. Zhu S, Yuille A. Region competition: unifying snakes, region growing, and Bayesian/MDL for multiband image segmentation. IEEE T Pattern Anal 1996;18:884–900.
21. Chan TF, Vese LA. Active contours without edges. IEEE T Image Process 2001;10:266–277.
22. Chan TF, Vese LA. A level set algorithm for minimizing the Mumford-Shah functional in image processing. Proc. 1st IEEE workshop on Variational and Level Set Methods in Computer Vision. Vancouver, Canada, 2001. p. 161–168.
23. Zhao H, Chan T, Merriman B Osher S. A variational level set approach to multiphase motion. J Comput Phys 1996;127:179–195.
24. Malladi R, Sethian JA, Vemuri BC. Shape modeling with front propagation: a level set approach. IEEE T Pattern Anal 1995;17:158–175.
25. Cheng J, Greiner R. Learning Bayesian belief network classifiers: algorithms and system. Proceedings of the 14th Canadian Conference on Artificial Intelligence. Ottowa, Canada, 2001, p. 141–C151.
26. Wasserman BA, Smith WI, Trout HH, Cannon RO, Balaban RS, Arai AE. Carotid artery atherosclerosis: in vivo morphologic characterization with gadolinium-enhanced double-oblique MR imaging—initial results. Radiology 2002;223:566–573.
27. Han C, Kerwin WS, Hatsukami TS, Hwang JN, Yuan C. Detecting objects in image sequences using rule-based control in an active contour model. IEEE T Biomed Eng 2003;50:705–710.
28. Saam T, Kerwin WS, Chu B, Cai J, Kampschulte A, Hatsukami TS, Zhao XQ, Polissar NL, Yarnykh VL, Flemming K, Huston J, Insull W, Morrisett JD, Rand SD, DeMarco KJ, Yuan C. Sample size calculation for clinical trials using magnetic resonance imaging for the quantitative assessment of carotid atherosclerosis. J Cardiovasc Magn Reson 2005; 7:799–808.